Development 140, 4051-4059 (2013) doi:10.1242/dev.090878
© 2013. Published by The Company of Biologists Ltd

A global pattern of mechanical stress polarizes cell divisions and cell shape in the growing *Drosophila* wing disc

Loïc LeGoff*, Hervé Rouault‡ and Thomas Lecuit*

SUMMARY

Organismal development is under genetic control. Ultimately, mechanical forces shape embryos. If we want to understand the precise regulation of size and shape in animals, we must dissect how forces are distributed in developing tissues, and how they drive cell behavior to shape organs. This has not been addressed fully in the context of growing tissues. As cells grow and divide, they exert a pressure on their neighbors. How these local stresses add up or dissipate as the tissue grows is an unanswered question. We address this issue in the growing wing imaginal disc of *Drosophila* larvae, the precursor of the adult wing. We used a quantitative approach to analyze the strains and stresses of cells of the wing pouch, and found a global pattern of stress whereby cells in the periphery of the tissue are mechanically stretched and cells in the center are compressed. This pattern has important consequences on cell shape in the wing pouch: cells respond to it by polarizing their acto-myosin cortex, and aligning their divisions with the main axis of cell stretch, thereby polarizing tissue growth. Ectopic perturbations of tissue growth by the Hippo signaling pathway reorganize this pattern in a non-autonomous manner, suggesting a synergy between tissue mechanics and growth control during wing disc morphogenesis.

KEY WORDS: *Drosophila*, Hippo signaling, Tissue growth, Tissue mechanics, Wing imaginal disc

INTRODUCTION

Tissues develop their shape through mechanical processes. Mechanical stress, the internal distribution of forces within cells and tissues, is what make cells move, change shape, or exchange neighbors. The mechanisms by which signaling pathways that pattern the embryo impact on the distribution of mechanical stress, and how this determines cell behavior have been the subject of intense focus recently (Heisenberg and Bellaïche, 2013). For example, during *Drosophila* gastrulation, a mechanical stress arising from polarized cell contractility powers cell-intercalation in the extending germ-band (Bertet et al., 2004; Rauzi et al., 2008; Zallen and Wieschaus, 2004). Likewise, cell intercalation drives extension of the neural tube in vertebrates (Nishimura et al., 2012).

Mechanical interactions differ from biochemical intercellular communication by their non-locality: mechanical perturbation spreads over large distances in a tissue owing to the transmission of tensions through tissue connectedness. Thus, mechanics could, in principle, act globally to coordinate morphogenesis. In this context, measuring patterns of mechanical stress in developing tissues and assessing their impact on cell behavior is one of the first steps necessary to understand morphogenetic processes.

Developmental mechanics have mostly been investigated in animal tissues that grow poorly, often in the context of gastrulation. Here, we study growing tissues that shape themselves as they grow. How growth impacts on the distribution of stress and subsequent shaping of tissues is not known. As a result, we understand poorly how shape and size are coordinated *in vivo* (Lecuit and Le Goff, 2007). Recent efforts have focused on the identification of growth factors, such as morphogens, and understanding of how they control cell behavior and proliferation (Wartlick et al., 2009). Yet morphogens cannot act alone. Growth is a mechanical process: each time a cell grows, new matter is being added within the tissue. Tissues do not always passively follow 'instructions' from morphogens. Indeed, if the tissue surrounding a growing cell cannot rearrange itself, it will resist this local perturbation, resulting in a local mechanical stress that, in return, constrains the dividing cell. As more divisions proceed, these local stresses may accumulate and give rise to a macroscopic stress that will affect tissue shape. Thus, as a result of cell-cell connectedness, a resultant growth emerges that differs from the one initially specified by morphogens. This is what happens in plants, in which cells cannot move and cannot exchange neighbors (Green et al., 2010; Kuchen et al., 2012). The opposite situation is that of loosely connected cells, which can make way for growth, resulting in an effective fluid flow where no mechanical stress is generated, as in cultured multicellular spheroids.

Where do animal tissues stand in this range of behavior? The occurrence of large-scale mechanical stress will depend on the balance between sources of stress and dissipation through cell rearrangements. Such a description of the mechanics of growing animal tissues is of prime importance but still awaits experimental assessment. A macroscopic stress might affect cell division or apoptosis and regulate signaling pathways. Recent work demonstrated the influence of tissue mechanics on activation of the Hippo pathway (Dupont et al., 2011; Fernández et al., 2011; Sansores-Garcia et al., 2011), and direct mechanical feedback has been demonstrated in the *Drosophila* thorax (Marinari et al., 2012) and in *Arabidopsis* meristem (Uyttewaal et al., 2012).

Here, we investigate the interplay between tissue mechanics and morphogenesis at the tissue level in the precursor of the *Drosophila* wing: the wing disc. This pseudo-stratified epithelium is a powerful system in which to study growth control and epithelial morphogenesis. It grows by a thousand-fold over 5 days under the control of the morphogens Decapentaplegic (Dpp) and Wingless

---

IBDML, UMR7288 CNRS-Université d'Aix-Marseille. Campus de Luminy, case 907, 13288 Marseille Cedex 09, France.

*Authors for correspondence (loic.le-goff@univ-amu.fr; thomas.lecuit@univ-amu.fr)
‡Present address: Institut Pasteur, Developmental Biology Department, F-75015 Paris, France

Accepted 19 July 2013

(Wg), which coordinate growth in synergy with the Hippo pathway (Baena-Lopez et al., 2012; Halder and Johnson, 2011; Oh and Irvine, 2011). We address the interplay between growth and tissue mechanics in the bulk of the wing disc. We find the existence of a global pattern of mechanical stress that impacts on tissue morphogenesis. We first analyze the mechanics of the developing precursor of the wing disc, then address its impact on tissue morphogenesis, and finally show that clonal perturbation of growth rates affects the mechanics of the tissue non-autonomously. We discuss the implications of these findings on the regulation of tissue stress during wing disc development.

MATERIALS AND METHODS

Fly stocks and genetics

E-cadherin (Shotgun) was visualized with ubi-E-cad::GFP, which rescues a null mutant (Oda and Tsukita, 2001). Myosin-II (MyoII) was visualized with a MyoII regulatory light chain (Sqh in *Drosophila*) GFP/cherry-fusion (Sqh::GFP or sqh::Cherry) under the *spaghetti-squash* promoter, which rescues a protein null sqhAX3 null mutant. Gal4 flip-out clones were made with the transgene act >y+>Gal4,UAS-GFP (Bloomington#4411). LexA flipouts were made with act >y+>LexA,LexAop-CD8::GFP, a recombinant of a LexA flipout (Schwank et al., 2011b) and Bloomington Stock Center #32203, a gift from C. Bertet (NYU, NY, USA). RNAi clones were generated with a UAS-*expanded*-dsRNA stocks from the TRiP project (Ni et al., 2008) with UAS-Dcr2, and observed 48 hours after heatshock. UAS-Yki clones (stock from P. Leopold, University of Nice, France) were observed 30 hours after heatshock. D::GFP was a gift from Y. Bellaiche (Institut Curie, Paris, France). Supplementary material Table S1 gives the genotypes for all figures.

Live imaging of wing discs

Discs were dissected from third instar larvae in clone 8 medium (shield and Sang medium supplemented with 2% FCS, 12.5 IU/100 ml insulin and 2.5% fly extract), and imaged in glass-bottomed Petri dishes. Images were collected using a spinning disc confocal (60×/W1.2NA lens). Voxels were 0.133×0.133×0.5 μm except for the analysis of cell divisions (0.266×0.266×1 μm to reduce illumination and phototoxicity). See supplementary material Movie 1 for a typical example of a movie. Figure 1C is based on two-photon imaging of fngGal4 >UAS-GFP to generate cross-sections of the pouch. Immunostaining [Dlg, Flamingo (Starry night) and α-catenin] was performed using a standard protocol (Klein, 2008). This study investigates the pouch of the wing disc. From mid-third instar onwards, the pouch is delineated by the existence of the deep folds around it. Before that (supplementary material Fig. S10, green curve), the pouch can be delineated by the expression of a vestigial Quadrant enhancer reporter (Zecca and Struhl, 2007). Compartment boundaries in the pouch are used to register data. Both compartment boundaries are visible, because cells reproducibly align along these straight boundaries by a mechanism that is associated with recruitment of MyoII.

Laser ablation

Single junction ablations were performed as published (Rauzi et al., 2008) using an infrared femtosecond laser to generate ablations. Ablations were performed both in the pouch periphery (>50 μm from the geometric center) and the medial region (<35 μm). Supplementary material Movies 2 and 3 show ablations on junctions parallel (supplementary material Movie 2) or transverse (supplementary material Movie 3) to the local axis of deformation (aligned to the *x*-axis).

Inhibition of Myosin-II

Wing discs were exposed to 1 mM Y27632 in clone 8 medium for 40 minutes. Inhibition was tested observing MyoII::GFP: treated discs show a clear reduction in junctional MyoII compared with control (supplementary material Fig. S1). To compare tissue morphometry before and after Y27632 treatments, wing discs were put in individual drops of clone 8 medium and imaged. Each drop was then supplemented with Y27632 to a final concentration of 1 mM. The discs were then re-imaged after an incubation time of 40 minutes.

Image analysis

Image analysis procedures are detailed in supplementary material Appendix S1. An important part was the statistical morphometry, which results in a collection of coarse-grained morphometric maps (apical area, orientation, ellipticity).

RESULTS

Tissue deformations are patterned in the wing pouch

Because forces impact on the shape of cells, we conducted a systematic analysis of cell shape in the presumptive wing blade, called the pouch. We cultured living third instar wing discs and imaged the contour of cells with an E-cadherin::GFP fusion (Fig. 1A). We developed image analysis tools to investigate the shape of cells, which sequentially: improve the signal-to-noise ratio of 3D projections; skeletonize the contour of cells; perform a statistical analysis of the shape of cells. Morphometric data were averaged both locally and among registered tissues (using the compartment boundaries as a reference). Averaging 17,000 cells over 15 discs of mid-third instar larvae, we obtained coarse-grained morphometric maps that reveal patterns of cell shape.

First, we measured a linear increase in the apical surface area from the center of the pouch to the periphery (Fig. 1B). This pattern is almost concentric. Its minimum coincides with the center of mass of the pouch, a few cell diameters anterior from the antero-posterior (AP) compartment boundary (Fig. 1B). As shown in supplementary material Fig. S6, the area distribution at a given distance from the center is broad. But with a large enough statistical population (n≈4500 for this particular distribution, which give rise to one point in Fig. 1B′), significant spatial variations emerge from our analysis. The apico-basal length of cells was, by contrast, greater in the center than in the periphery (Fig. 1C). This suggests that cells in the center do not have a smaller volume than those in the periphery (Fig. 1C), but have a different shape. On mechanical grounds, this change in aspect ratio could have two different causes. Cells in the center might actively constrict their apical surface, or alternatively they might be laterally compressed by the surrounding peripheral cells of the pouch, while keeping their volume constant. These models make different predictions about the shape of cells in the periphery. If central cells contract their apical surface, then peripheral cells should be stretched radially towards the central contraction. However, if central cells are compressed by the peripheral ones, then conversely peripheral cells should be stretched tangentially in order to equilibrate stress. We analyzed local tissue orientation using the texture matrix (Graner et al., 2008) (supplementary material Appendix S1, equation 2) (Fig. 1D) and found that it is also strongly patterned in the wing pouch. The coarse-grained map of local orientation (Fig. 1E) shows two interesting features. First, there is a gradual tendency from the center to the periphery to orient the tissue tangentially (Fig. 1E,F); this tendency was only interrupted at the compartment boundaries along which the tissue locally aligns. Second, the amplitude of deformations along the axis of orientation increases from the center of the tissue to the periphery: the tissue is isometric in the center and becomes gradually anisotropic towards the periphery (Fig. 1G). Together, these observations argue that cells are stretched at the periphery and might be compressed at the center. The orientation of cells at the periphery suggest that these internal stresses are the consequence of a force balance whereby peripheral cells compress cells in the center and cells in the center stretch cells in the periphery. If these morphometric patterns emerge from a single underlying pattern of mechanical stress, they should tightly overlap. Indeed, the center of symmetry of the apical area pattern

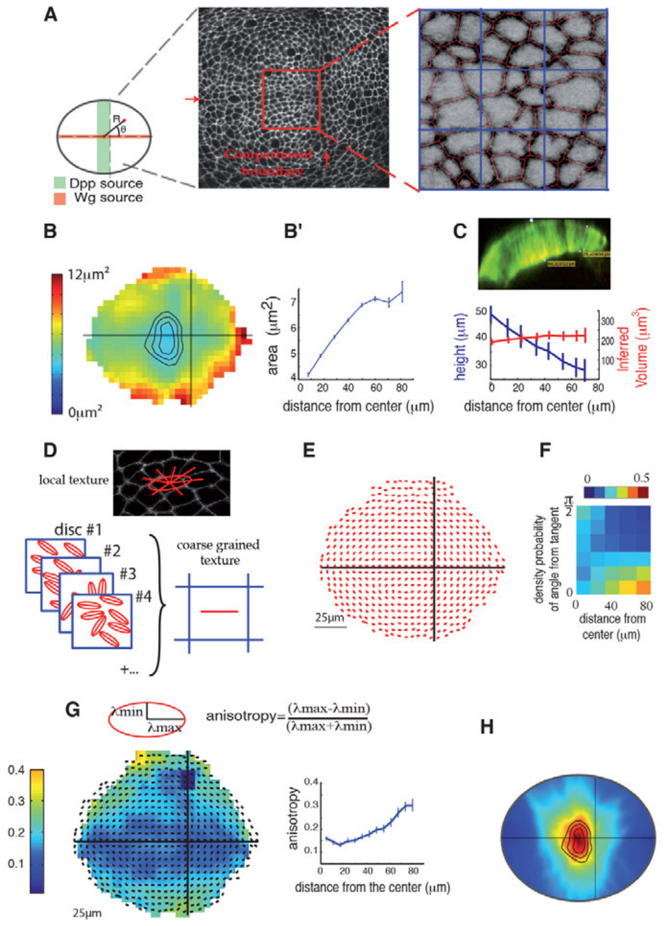

Fig. 1. Patterned cell deformations in the wing precursor. (**A**) Left: Schematic of a *Drosophila* wing pouch, with the two sources of morphogens, Dpp and Wg, abutting the compartment boundaries (dashed lines). We use polar coordinates for which the center is defined as the common center of morphometric maps (see H). Center: Image of an E-cad::GFP wing pouch . Images of different discs are registered using the compartment boundaries as landmarks (red arrows). Right: The E-cadherin::GFP signal (inverse grayscale) is skeletonized (red outline). Morphometry is coarse-grained in 5-μm bins (blue grid). (**B**) The map of apical cell area shows a concentric pattern. Black curves are contour lines near the minimum used in G. (**B′**) Quantified area as a function of the distance to the center. (**C**) A section of the tissue along the dorsoventral compartment boundary shows a correlated pattern in cell height (cells are higher in the center). (**D**) Local tissue orientation is computed around cells using the texture tensor. (**E**) The coarse-grained map of orientation shows an alignment of cells along compartment boundaries, and a concentric organization. (**F**) Angular distribution of tissue orientation with respect to the local tangent shows no preferred orientation in the center and a gradual tangent orientation towards the periphery. (**G**) Map of tissue anisotropy: cells in the periphery are more anisotropic (the orientation shown in E was superimposed). (**H**) Superposition of the area map (contour lines, same as in B) and the density of bisector of the orientation map (heatmap; see supplementary material Appendix S1 and Fig. S3 for justification that it relates to the center of the orientation pattern) shows a good alignment. Error bars represent s.e.m.

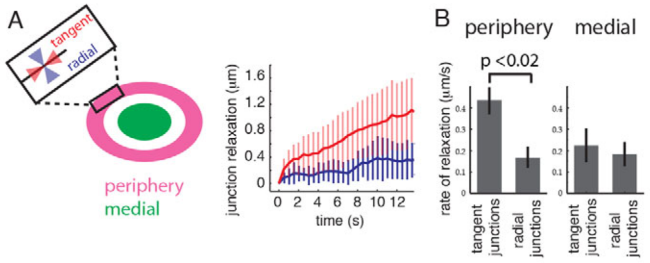

Fig. 2. Direct measurement of junctional tension confirms the existence of mechanical stress. (**A**) Ablation in the pouch periphery. Junctions were classified as either tangent (red) or radial (blue). Tangent junctions relax faster than radial ones. (**B**) Initial recoil velocity for the tangent and radial junctions in the periphery of the pouch (distance >50 μm from the center) indicate an increased tension on the former. In the medial region (distance <35 μm from the center), there is no significant difference between tangent and radial junctions. Error bars represent s.e.m.; *P*-value from Kolmogorov-Smirnov (KS)-test.

(Fig. 1B,H, contour lines) coincides with the center of symmetry of the deformation pattern (Fig. 1H, color code, visualized with the density of bisectors introduced in the appendix and the supporting supplementary material Fig. S3). Thus, our statistical morphometry revealed a pattern of cell deformation that suggests the existence of a global pattern of mechanical stress. Interestingly, the center of mass of the pouch coincides with the center of symmetry of tissue deformations.

Anisotropic force distribution reveals a tissue-level pattern of mechanical stress

In order to test our prediction that cells in the periphery of the pouch are under a tangential mechanical stretch, we performed laser-ablation experiments. In an epithelium, apical junctions concentrate most of the interfacial tensile activity (Farhadifar et al., 2007; Rauzi et al., 2008). We directly measured the distribution of tension by measuring the recoil velocity of individual junctions after ablation with a near-infrared femtosecond-pulsed laser (Rauzi et al., 2008). We classified junctions in two categories: tangent junctions that made an angle 0±30° with the local tangent of the geometrical elliptic approximation, and radial junctions (90±30° with the local tangent) (Fig. 2A). The initial recoil velocity was 2.5-fold higher for tangential than for radial junctions in the periphery (>50 μm from the center; Fig. 2B, left). Such a polarity was not observed in medial regions of the pouch (<35μm from the center) and the tension in this medial region was also lower (Fig. 2B, right). Our experimental observations show that cells in the periphery of the tissue are stretched anisotropically.

The stress pattern is independent of Dachs-mediated planar polarity

This led us to investigate the mechanisms of tangential stretching. The Fat/Dachsous planar polarity pathway is important for wing pouch morphogenesis (Baonza and Garcia-Bellido, 2005; Mao et al., 2006; Sagner et al., 2012). Downstream of Fat is the atypical myosin Dachs. Dachs has been shown to control cell edge tension in the pupal thorax and the wing disc (Bosveld et al., 2012; Mao et al., 2011). It is planar polarized in the wing disc at the junction level, with one side of each cell-cell junction containing more Dachs, along a proximo-distal gradient (Fig. 3A, left-hand schematic) (Ambegaonkar et al., 2012; Mao et al., 2006; Schwank et al., 2011b). Dachs has also been proposed to be polarized in the wing disc at the cellular level, with tangent junctions being enriched compared with radial junctions, leading to a radial bias in cell shape (Fig. 3A, right-hand schematic) (Mao et al., 2011). Dachs could thus be required for polarized cell stretching in the disc periphery. These

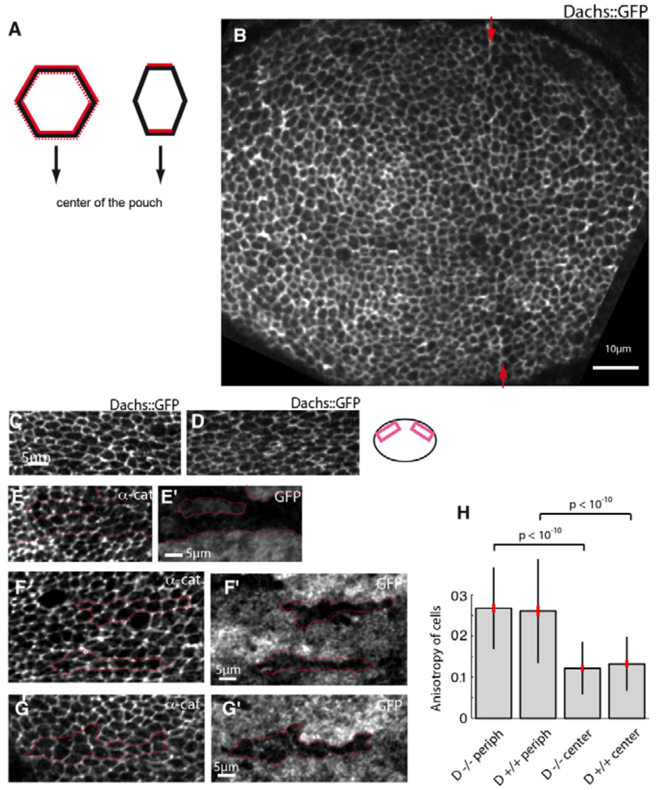

Fig. 3. Dachs planar polarity does not generate the stretch. (**A**) Reported polarity of Dachs in the pouch. Left: Dachs is polarized at the junction level. Junctions bear more Dachs on one side than the other (continuous versus dashed red lines). A polarity at the level of the cell is not necessarily seen. Right: Dachs is polarized at the level of the cell, yielding an asymmetry of cell shape. (**B**) No polarity is visible in a *dachs*$_{prom}$-Dachs::GFP reporter. Red arrows indicate anteroposterior compartment boundary. (**C**,**D**) Magnification of periphery (see schematic on the right) shows no polarity. (**E-G′**) *dachs*^{GC13} mutant cells in the periphery are as stretched as their WT neighbors. Mutant clones, labeled by absence of GFP, are outlined (E′-G′). (**H**) Quantification confirms that *dachs*$^{-/-}$ cells are as anisotropic as their non-mutant neighbors. Black error bars represent s.d.; red error bars represent s.e.m.; *P*-values are from KS test.

polarity measurements were made by overexpressing V5-tagged Dachs in clones. To analyze Dachs polarity in relation to the stress pattern that we report, we imaged a Dachs::GFP fusion under the control of its endogenous promoter, which rescues a null mutant (Bosveld et al., 2012). Observation of Dachs distribution in the wing did not reveal any polarity of Dachs at the cellular level (Fig. 3B). This was confirmed by higher magnification of peripheral regions (Fig. 3C,D), where Dachs is unpolarized. We conclude that the junctional polarity of Dachs does not give rise to a significant cellular-level polarity, the low level on one side of a junction being probably compensated by the higher levels on the other side of the same junction in the neighboring cell. We further tested functionally the role of Dachs by looking at cell shape in *dachs*^{GC13} mutant clones, carrying a loss-of-function mutation that results in a phenotype similar to that of the null mutant (Mao et al., 2006). We observed that cells were stretched like their wild-type (WT) neighbors (Fig. 3E-H), thus supporting the view that the stretch is not dependent on Dachs motor activity. Together, our results are inconsistent with, and argue against, a model in which a polarized enrichment of Dachs at the cellular level would bias cell shape and give rise to the pattern of stress at the disc periphery.

MyoII forms polarized supracellular cables in the periphery of the tissue

Cells reorganize their acto-myosin cytoskeleton upon mechanical stimulation. This has been reported on isolated fibroblasts and *Dictyostelium* (Effler et al., 2006; Yoshigi et al., 2005), cell aggregates (Guevorkian et al., 2011) and in *Drosophila* embryos (Fernandez-Gonzalez et al., 2009). We looked for a possible signature of mechanical stretch in the cytoskeleton of cells. We used a fusion of Myosin-II (MyoII) regulatory light chain and GFP (or Cherry when co-visualized with E-cad::GFP) to inspect the cell cortex at apical junctions. We extracted the signal at adherens junctions of pouch cells using selective plane projection (supplementary material Appendix S1 and Fig. S2). Contrary to Dachs, MyoII::GFP was enriched in a polarized manner in the periphery, forming supracellular cables of enrichment tangent to the wing pouch (Fig. 4A). This was not observed in the center of the pouch (Fig. 4A). The MyoII cables were not associated with a local enrichment of E-cad::GFP (Fig. 4B). Polarized MyoII in the periphery also contrasted with unpolarized Dachs (Fig. 4C,D; Fig. 3), an observation confirmed by the co-visualization of MyoII::Cherry and Dachs::GFP (Fig. 4E). Quantification of the angular distribution of MyoII confirmed the polarized distribution of MyoII (Fig. 4F). The formation of MyoII cables also correlated with a modification of the shape of cells, which became slightly more rectangular (quantified by the angular distribution of junctional length with respect to the axis of the cable; Fig. 4G). Cells in the periphery, however, were still topological hexagons on average (supplementary material Fig. S7). Polarized enrichment of MyoII in cells abutting the compartment boundaries, leading to changes in cell shape, have been reported (Landsberg et al., 2009; Major and Irvine, 2006). Our results show that these singular mechanical properties at the compartment boundaries are also present in the bulk of the tissue.

MyoII cables are induced in response to mechanical stress of the tissue

MyoII cables are localized at the periphery of the wing pouch, where the tissue is stretched and similarly orients tangentially (see supplementary material Fig. S8 for a qualitative assessment). This suggests a link between cell stretching and MyoII polarity. We addressed this at the subcellular level using laser ablation in cells expressing E-cad::GFP and MyoII::Cherry. We defined a polarity index, which measures how much a junction recruits MyoII relative to its neighbors, and is >0 for junctions that are part of the MyoII cables and <0 for the dim transverse junctions (mathematical definition in equation 8 of supplementary material Appendix S1). We found that the speed of relaxation after ablation correlated positively with the polarity index (Fig. 5A). Thus, junctions that are part of the enriched cables are more tensed than their transverse counterparts.

These results establish a correlation but do not demonstrate a causal link. MyoII polarity may be a cause or a consequence of cell deformation. Alternatively, both might be controlled independently by an upstream signal. To address this, we investigated the effect of MyoII inactivation using the ROCK inhibitor Y27632 (Bertet et al., 2004; Farhadifar et al., 2007) (see supplementary material Fig. S1 for assessment of efficiency of inhibition). We first probed junctional tension after ROCK inhibitor treatment using laser ablation. MyoII::GFP was totally removed from junctions in the presence of Y27632 (Fig. 5C). Overall, recoil velocity decreased

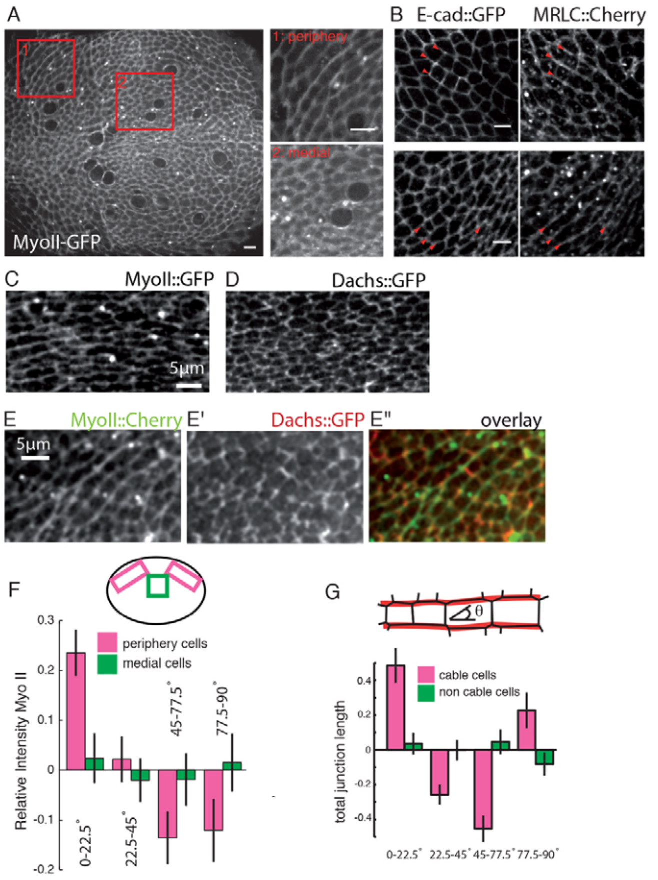

Fig. 4. MyoII enrichment in stretched regions. (**A**) MyoII-GFP in the pouch. Insets: Polarized enrichment in periphery but not in medial regions. (**B**) E-cad-GFP and MyoII-Cherry co-visualization shows absence of E-cad polarity in cables (arrowheads). (**C**,**D**) MyoII polarity contrasts with Dachs absence of polarity even in the periphery (D, same as Fig. 3D). (**E-E″**) Co-visualization of Dachs::GFP and MyoII::Cherry confirms MyoII polarity in the absence of Dachs polarity. (**F**) Angular distribution of junctional MyoII shows a polarity in the periphery (magenta) but not in the medial region (green). Angles are measured with respect to the average tissue orientation. Relative intensity is normalized by the mean $I_i^r=(I_i-I_{mean})/I_{mean}$ (supplementary material Appendix S1, equation 6). (**G**) Summed length of junctions as a function of the angle made with the axis of the cables. Junctions perpendicular or tangent to the cables dominate the distribution, thus giving cells rectangular shapes. Summed length of junctions is expressed in relative normalized length $L_i^r=(L_i-L_{mean})/L_{mean}$ (supplementary material Appendix S1, equation 7). For control (green), strings of cells were arbitrarily handpicked in the medial region. Error bars represent s.e.m. Scale bars: 5 µm.

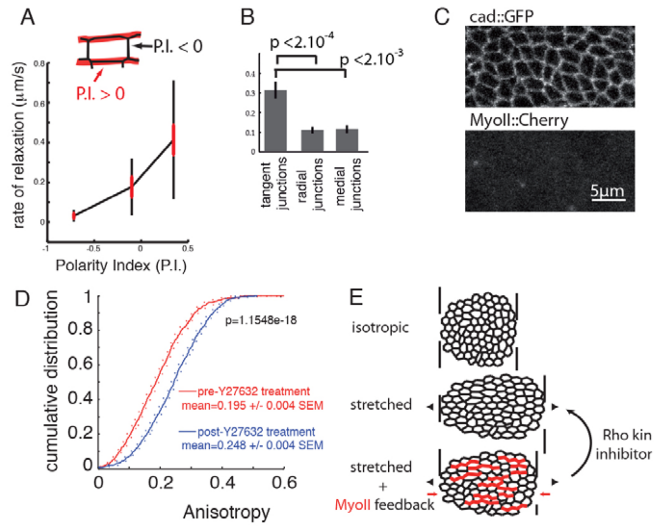

Fig. 5. Linking MyoII enrichment and mechanical stress. (**A**) Junctional recoil velocity after ablation versus polarity index shows that MyoII enrichment correlates with cortical tension. Black error bars represent s.d.; red error bars represent s.e.m.; *P*-values are from KS test. (**B**) Recoil velocity after Y27632 treatment. The polarity in the periphery is still observed as indicated by the different recoil for radial and tangent junction. Medial junctions are also still significantly less tensed than tangent peripheral ones. Error bars represent s.e.m.; *P*-values are from KS-test. (**C**) Region of interest in a disc treated with Y27632 at the level of the adherence plane: MyoII has been removed from junctions. (**D**) Tissue anisotropy in peripheral regions before and after Y27632 treatment. The cumulative distribution shows a small but significant increase in anisotropy after treatment. (**E**) Model for MyoII polarity: the stretch at the periphery polarizes MyoII (red lines), resulting in a small reduction of anisotropy (red arrows). The tissue goes back to its basal mechanical stretch after MyoII inhibition.

significantly upon treatment (ratio of mean velocity without/with inhibition=1.45; significance of the difference: P=0.025). However, the polarity of stress was still observed in the peripheral junctions: tangent junctions were still more tensed than radial ones (Fig. 5B). Accordingly, the apical surface of cells in the center of the pouch was still smaller than that of cells in the periphery (supplementary material Fig. S9). Thus, the stretch in the periphery does not seem to rely on MyoII tensile activity at the junctions. This supports the idea of a mechanical loading of cells in the periphery by a pattern of stress. We also analyzed the shape of cells after MyoII inactivation. We observed a small increase of tissue deformation in the periphery [pre-inhibition: 0.195±0.006 (mean ± s.e.m.); post-inhibition: 0.248±0.006; $P<10^{-6}$; Fig. 5D]. This is inconsistent with the idea that MyoII polarity is the cause of cell stretching, which predicts a reduction of cell stretching upon ROCK inhibition. Because the stretch does not rely on Dachs, and because MyoII cables strongly correlate with the stretch, we also do not favor a hypothesis linking MyoII cables and planar polarity pathways. Instead, we propose that MyoII polarity is a consequence of cell stretching. Because this polarized enrichment results in cells being slightly less stretched, it acts as a negative mechanical feedback that limits tissue deformation (Fig. 5E).

Cell divisions are re-oriented parallel to the lines of stress

Next, we investigated the consequence of tissue stretching on the mitotic behavior of cells. Local tissue deformation is associated with an elongation of cells. We tested whether the pattern of cell divisions in the wing pouch emerges in part from the tissue level mechanical state via cell elongation. Cell divisions were observed on time-lapse movies of cultured discs spanning 8 hours of development (supplementary material Movie 1). Registering divisions using compartment boundaries, we quantified their orientation at the exit from mitosis. In the center of the tissue, the orientation of divisions is predominantly radial (Fig. 6A). This confirms earlier reports documenting control of division orientation by the planar polarity Ft/Ds pathway mediated by the atypical myosin Dachs (Baonza and Garcia-Bellido, 2005; Mao et al., 2011). However, this polarity

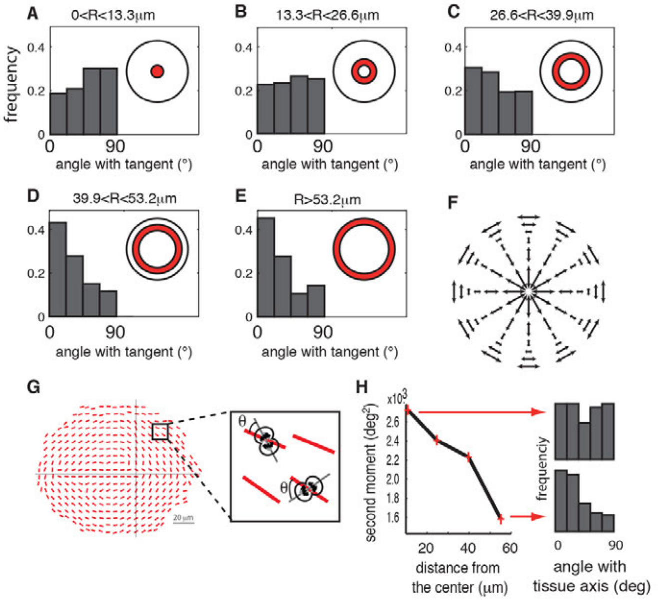

Fig. 6. Orientation of cell divisions in the wing pouch. (**A-E**) Orientation of cell divisions (with respect to tangent) in concentric circles spanning the wing pouch. Divisions become gradually tangent in the periphery. Histograms represent the normalized angular distribution. (**F**) Illustration of the pattern divisions. Divisions are radial in the center and tangent in the periphery. Length of arrows reflects the degree of polarity. (**G**,**H**) Direct comparison of the orientation of divisions and the local tissue axis. The second moment of the angular distribution is plotted against the distance to the center of the tissue. Two distributions (center versus periphery) are represented on the right.

vanishes further from the center (Fig. 6B) and eventually rotates 90° as it becomes tangential in the peripheral regions (Fig. 6C-E) (Baonza and Garcia-Bellido, 2005) (see Fig. 6F for a schematic of the pattern of cell divisions). Interestingly, the orientation of divisions correlated with local tissue deformation in the periphery, but not in the center: the variance of the angles of cell division with respect to the local tissue deformation (Fig. 6G) gradually decreases from the center to the periphery (Fig. 6H). Although these correlative measurements do not strictly demonstrate causation, they nevertheless suggest that the mechanical state of the tissue biases cell division orientation: the more anisotropic the tissue is, the more coherently divisions orient along the axis of stretch. Two different cues would then bias the orientation of cell divisions in the wing pouch: Dachs polarity would induce radial cell divisions in the center of the pouch (Mao et al., 2011), and mechanical stretch would induce tangent cell divisions in the periphery. Such an orientation of divisions along the stretch dominates stress-releasing processes in the wing pouch, as cell-intercalations are scarce. Indeed, we quantified cell intercalation events by tracking pairs of cells in 5- to 8-hour-long movies (supplementary material Movie 1). Discarding pairs that led to the division of one of the two cells, we found that about 1% of 450 pairs were disconnected by an intercalation event, thus confirming the finding of (Gibson et al., 2006) that cell exchanges are scarce in the pouch.

Ectopic alterations of Hippo signaling induce non-autonomous stress reorganization

As explained above, growth could, in principle, induce mechanical stress (Green et al., 2010). Only growth that is both completely homogeneous in space and orientation does not induce mechanical stress in a tissue. Growth is reported to be globally fairly uniform (Milán et al., 1996; Schwank et al., 2011b; Wartlick et al., 2011b). However, some heterogeneity has been reported by O'Brochta and Bryant, who observed, in addition to the reduced proliferation at the dorsoventral (DV) boundary, a reduced proliferation in the periphery 96 hours after egg laying (O'Brochta and Bryant, 1985). Whether growth is homogeneous remains an unanswered question, in particular because it is cell divisions that are usually measured (by counting mitotic cells), not growth. We assessed a potential link between growth and mechanics perturbing growth patterns. The Hippo pathway is required for growth control in imaginal discs (Halder and Johnson, 2011; Huang et al., 2005; Tapon et al., 2002). We inactivated Hippo signaling to induce local over-growth within flip-out clones by knocking down the gene *expanded*, which encodes for a activator of the pathway (Boedigheimer and Laughon, 1993; Halder and Johnson, 2011), or overexpressing the transcription factor Yorkie (Yki), which results in transcriptional activation of cell growth (Huang et al., 2005). Both experiments induced similar, non-autonomous effects on cell shape. Cells inside the clone tended to be isotropic and had a smaller apical surface, whereas cells in the WT surrounding tissue were larger and anisotropic, with their main axis oriented in a tangent angle with respect to the border of the clone (Fig. 7A-B). Quantification of local tissue deformation shows a systematic increase of tissue anisotropy and apical area from the center of the clone to the surrounding tissues (Fig. 7B). Interestingly, *expanded*-RNAi clones could also re-polarize MyoII, acting as an organizing center for MyoII cables, which formed swirling patterns around the clone (Fig. 7C). Similar effects were observed after Yki overexpression (Fig. 7D). These results suggest that alteration of growth (overgrowth in this case) can recapitulate, at a mesoscopic level, the global patterns of stress that we observe in the entire wing disc. We qualitatively confirmed this non-autonomous mechanical perturbation of WT tissue surrounding Yki overexpression at a mesoscopic level using a two-clones protocol. We induced both WT LexA flip-out clones (labeled with a membrane GFP) and Yki overexpressing Gal4 flip-outs (cytosolic GFP). Figure 7E shows that the Yki-overexpressing clone was overgrown compared with surrounding WT clones. Furthermore, the WT clones neighboring the Yki-overexpressing clones were bent and globally distorted (Fig. 7E). Although we cannot exclude a contribution from apical F-actin enrichment upon Hippo modulation (Fernández et al., 2011), our experiments on *expanded* and *yorkie* are consistent with the generation of a local overpressure by overgrowing clones.

DISCUSSION

Mechanical stress in the wing disc

Our first result is that the precursor of the *Drosophila* wing experiences mechanical stress far beyond the compartment boundaries in the course of its development. We found that the peripheral region of the wing pouch is stretched tangentially (i.e. parallel to the presumptive hinge). Although mechanical stress has been shown to play a role in a range of morphogenetic processes such as gastrulation (Butler et al., 2009; Rauzi et al., 2008) or planar cell polarity (PCP) (Aigouy et al., 2010; Olguín et al., 2011), the context of a growing wing disc raises a new question: how do the constant cell rearrangements provided by cell divisions affect the distribution of stress in the tissue? It was proposed on theoretical grounds that divisions dissipate mechanical stress, maintaining the tissue in a stress-free, liquid-like state (Ranft et al., 2010). Our observations show that this is not the case in the wing pouch.

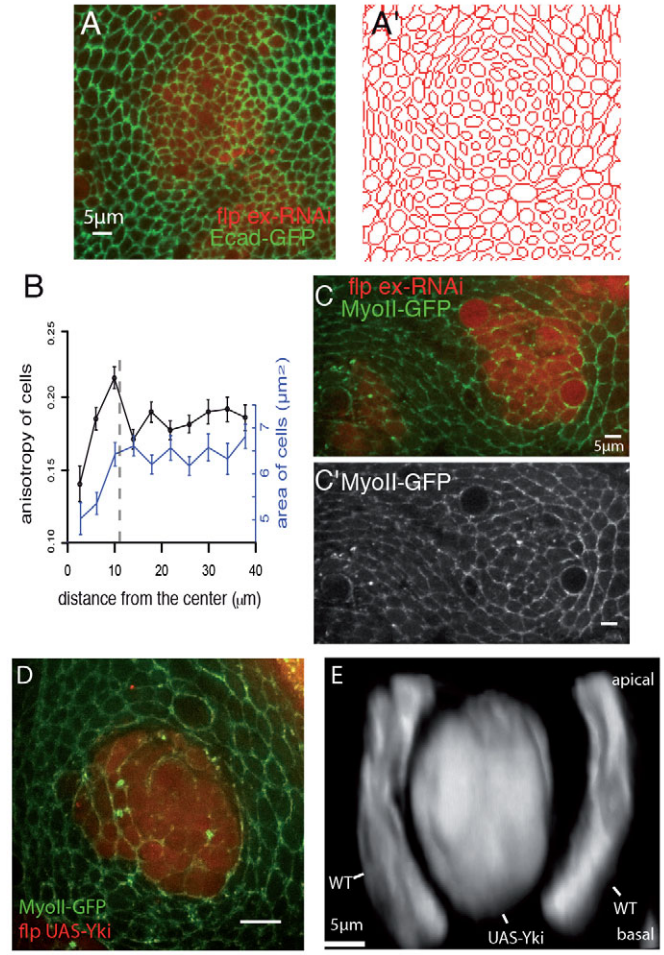

Fig. 7. Ectopic overgrowth induces tissue strain. (**A**,**A′**) An *expanded* RNAi clone induces a non-autonomous deformation of the tissue. The texture (A′) shows the deformation both inside and outside of the clone. (**B**) Quantification of the anisotropy and apical size of cells induced by *expanded* RNAi, averaged over five representative clones. Distance is from the center of the clones. Dashed line shows average clone size. Error bars represent s.e.m. (**C**,**C′**) MyoII reorganization around an *expanded* RNAi clone. (**D**) A UAS-Yki flip-out clone polarizes the surrounding tissue. (**E**) Side view of a UAS-Yki flip-out clone surrounded by WT clones. The WT clones are distorted by the Yki-induced overgrowth. Scale bars: 5 µm.

Although stress dissipation by divisions is likely to be at play in the pouch, notably in the form of cell divisions oriented along the axis of stretch (see below), it is not sufficient to completely dissipate the stress. The apparent absence of exchange of neighbors in this tissue during larval development (our data) (Gibson et al., 2006) is also expected to contribute to a low dissipation of stress. The fact that proliferation slows down during the third instar stage, might also explain this insufficient dissipation of stress. Interestingly, the amplitude of mechanical stress seems to increases in that same time window (supplementary material Fig. S10). In plants, the growing meristem is brought even further from mechanical equilibrium by positive feedback between mechanics and growth, resulting in shape-generating instabilities (Uyttewaal et al., 2012). Thus, preventing the tissue from dissipating mechanical stress might be a general way to generate shape. The existence of stress in the wing pouch might play a role in polarizing mechanics for subsequent changes (for example, when the tissue acquires its 3D shape, a process known as evagination). Polarized stress and polarized MyoII might impact on the extension of the whole pouch along the proximo-distal axis, which proceeds during evagination and is also thought to depend on cell exchanges (Condic et al., 1991; Fristrom, 1976).

How cells respond to stretch: Impact of mechanics on morphogenesis

At a local scale, cells respond to stretch by polarizing their cytoskeleton (Figs 4, 5) and orienting their divisions (Fig. 6). The fact that cells respond to stretch by polarizing their cytoskeleton has two implications on the cellular lattice of the tissue. First, it serves as a homeostatic mechanism: by stiffening or contracting their cortex along the axis of stretch, cells reduce the deformation they undergo (Fig. 5D,E). Second, it leads to the emergence of higher order structures in which cells assemble linearly along MyoII cables. These cables are akin to those found at compartment boundaries and might limit cell mixing in the bulk of the tissue or participate in orienting cell divisions there. Overall, the presence of mechanical stress, and the active response mediated by MyoII polarity, gives a representation of the cellular lattice that contrasts with the classic view inherited from Lewis, in which the shape of cells is on average hexagonal owing to their tendency to have six neighbors (Gibson et al., 2006; Lewis, 1926): in the periphery of the pouch, the shape of cells is driven by stress fields and not by topology.

A number of studies have reported the impact of cell shape and/or mechanical tension on the orientation of cell divisions in cultured mammalian cells (Fink et al., 2011; Théry et al., 2005), sea urchin (Minc et al., 2011), plants (Besson and Dumais, 2011), and the *Drosophila* wing disc (Gibson et al., 2011). The mechanisms at play in these various systems are likely to be different. Plants respond to mechanical stress by polarizing cell-wall stiffness (Uyttewaal et al., 2012). Cultured cells are polarized by forces conveyed by retraction fibers (Fink et al., 2011). In wing disc, Gibson and colleagues identified a regulation of the spindle axis associated with the local packing geometry (Gibson et al., 2011). Our results extend these findings by showing that a pattern of mechanical stress conveys a pattern of spindle orientation, potentially through the same mechanism. In the wing disc, the mitotic spindle undergoes rounds of rotations before final orientation is set. It can explore the mechanical energy landscape and may settle for an optimized orientation. Such alignment of divisions with the axis of stress could enhance the dissipation of stress discussed above.

Although stretch seems to control the orientation of divisions in the periphery of the tissue, this is not the case in the center of the pouch where cells are isometric (Fig. 1G). There, we find that divisions are predominantly radial, in agreement with published works that showed that the main operator of radial growth orientation in the center is the Fat/Dachsous/Dachs planar polarity pathway (Baonza and Garcia-Bellido, 2005; Mao et al., 2011).

The origin of mechanical stress

What is the source of mechanical stress in the tissue? Could patterning of cytoskeletal motor proteins yield regional differences in the shape of cells? To address this question, we looked at the distribution of the myosin motors MyoII and Dachs in the pouch. In the case of MyoII, and as discussed above, we did observe a polarity, but it is a response to stretch, not the direct cause. The stretch is still present after MyoII inactivation (Fig. 5B-D). In the case of Dachs, it was recently reported to be enriched in tangential junctions throughout the wing pouch, and proposed to increase their tension, resulting in a radial bias of cell shape (Mao et al., 2011). We thus assessed Dachs localization using a recent protein fusion under the control of the endogenous promoter (Bosveld et al., 2012). Based on our results that Dachs is apparently not polarized in the pouch and that Dachs mutant cells are anisotropic like their WT neighbors in the periphery, we conclude that Dachs is not a direct cause of the stretch (although it could contribute in a non-autonomous manner by polarizing growth in the center, see below). Our results on polarity, which may seem at odds with the published literature, are not necessarily so. There is significant evidence for the activity of Dachs to be polarized. It was shown that, at the single-junction level, Dachs enriches one side more than the other along a distal-to-proximal gradient (Ambegaonkar et al., 2012; Mao et al., 2006; Schwank et al., 2011a). Our observations were not designed to resolve such a polarity (we could not resolve individual sides of a junction). We do, however, observe that Dachs is not polarized at the cellular level, which fits with the isotropic cell shapes we observe in the center of the pouch. Mao et al. reported radial cells in the center (Mao et al., 2011), but did so only for anaphase cells, whereas we measured cell shape at all phases of the cell cycle, which could explain the discrepancy. More observations will be needed to dissect the mechanism by which Dachs polarizes growth radially in the wing pouch. Brittle et al. observed a cellular-level polarity of Dachs near the hinge region at very late stages of larval development (Brittle et al., 2012). Although we find that Dachs is not polarized at earlier stages and that it is not required for cell stretching (Fig. 3), we cannot exclude the possibility that Dachs might have a role at later stages when the tissue stops growing and starts evaginating. At these late stages, Dachs might induce polarized exchange of neighbors in the evaginating wing, as reported in the pupal notum (Bosveld et al., 2012).

The observation that cells are stretched in the periphery and compressed in the center could be simply explained on pure mechanical principles if expansion of central regions of the tissue was constrained by the periphery. This could occur if the rate of growth was stronger in the center than in the periphery; for example, by a gradual slowing down of growth in the periphery of the tissue. The cellular processes normally associated with tissue growth can thus have contrasting effects on mechanics: heterogeneous distribution of the rate or polarity of mass increase can be a source of mechanical stress, but cell divisions oriented in the axis of stretch introduce rearrangements that can dissipate stress. Although studies have measured homogeneous proliferation rates in the wing disc (Milán et al., 1996; Wartlick et al., 2011b), an earlier report emphasized declining proliferation rates from the center to the periphery (O'Brochta and Bryant, 1985). Our observations that perturbations of tissue growth by the Hippo signaling pathway leads to non-autonomous alteration of stress patterns (Fig. 7) is consistent with this and indicates that overgrowth can effectively induce non-autonomous tissue deformations similar to those observed in the wild type at the periphery. Importantly, the orientation of growth might be as important as the rate of growth. Cell divisions are oriented proximo-distally in the center of the pouch (see above). Such a pattern of orientation could also generate compression of the center and stretching of the periphery. A third potential mechanism would link mechanical stress in the periphery with the formation of the deep folds around the wing pouch that occurs in the course of late larval wing disc development (third instar). Cells that are invaginating might exert a pulling force that would result in patterns of mechanical stress akin to the one we observe. All the aforementioned mechanisms (rate/orientation of growth, mechanics of folds) are not mutually exclusive and could all contribute to shaping the pattern of stress we observe.

To conclude, non-local mechanical interactions lead to a global pattern of mechanical stress that feeds back on tissue morphogenesis in the periphery of the wing pouch. We did not measure how much this interplay between growth and mechanics contributes to the final size and shape of the wing. Future studies will have to address this. It will also be important to overcome the present limitations in measuring growth rates and orientation in living tissues in order to address this question.

Acknowledgements
We thank C. Bertet, M. Mavrakis, Y. Bellaiche and P. Leopold for stocks; and O. Wartlick, A. Kicheva and M Gonzalez-Gaitan for teaching disc cultures. Members of the Lecuit and Lenne group at IBDML contributed important discussions and commented on the manuscript.

Funding
This project was supported by the Centre National de la Recherche Scientifique (CNRS) [T.L. and L.L.G.]; the CNRS 'prise de risque' program [L.L.G.]; the Fondation Recherche Médicale (FRM) Equipe Labelisée [T.L.]; and the Association pour la Recherche sur le Cancer (Programme ARC). H.R. was supported by the FRM.

Competing interests statement
The authors declare no competing financial interests.

Author contributions
L.L.G. and T.L. designed the project ; L.L.G. performed experiments; L.L.G. and H.R. analyzed experiments; L.L.G., H.R. and T.L. interpreted the results and wrote the paper.

Supplementary material
Supplementary material available online at
http://dev.biologists.org/lookup/suppl/doi:10.1242/dev.090878/-/DC1

References

Aigouy, B., Farhadifar, R., Staple, D. B., Sagner, A., Röper, J.-C., Jülicher, F. and Eaton, S. (2010). Cell flow reorients the axis of planar polarity in the wing epithelium of Drosophila. *Cell* **142**, 773-786.

Ambegaonkar, A. A., Pan, G., Mani, M., Feng, Y. and Irvine, K. D. (2012). Propagation of Dachsous-Fat planar cell polarity. *Curr. Biol.* **22**, 1302-1308.

Baena-Lopez, L. A., Nojima, H. and Vincent, J.-P. (2012). Integration of morphogen signalling within the growth regulatory network. *Curr. Opin. Cell Biol.* **24**, 166-172.

Baonza, A. and Garcia-Bellido, A. (2005). The orientation of cell divisions determines the shape of Drosophila organs. *Curr. Biol.* **15**, 1640-1644.

Bertet, C., Sulak, L. and Lecuit, T. (2004). Myosin-dependent junction remodelling controls planar cell intercalation and axis elongation. *Nature* **429**, 667-671.

Besson, S. and Dumais, J. (2011). Universal rule for the symmetric division of plant cells. *Proc. Natl. Acad. Sci. USA* **108**, 6294-6299.

Boedigheimer, M. and Laughon, A. (1993). Expanded: a gene involved in the control of cell proliferation in imaginal discs. *Development* **118**, 1291-1301.

Bosveld, F., Bonnet, I., Guirao, B., Tlili, S., Wang, Z., Petitalot, A., Marchand, R., Bardet, P.-L., Marcq, P., Graner, F. et al. (2012). Mechanical control of morphogenesis by Fat/Dachsous/Four-jointed planar cell polarity pathway. *Science* **336**, 724-727.

Brittle, A., Thomas, C. and Strutt, D. (2012). Planar polarity specification through asymmetric subcellular localization of Fat and Dachsous. *Curr. Biol.* **22**, 907-914.

Butler, L. C., Blanchard, G. B., Kabla, A. J., Lawrence, N. J., Welchman, D. P., Mahadevan, L., Adams, R. J. and Sanson, B. (2009). Cell shape changes indicate a role for extrinsic tensile forces in Drosophila germ-band extension. *Nat. Cell Biol.* **11**, 859-864.

Condic, M. L., Fristrom, D. and Fristrom, J. W. (1991). Apical cell shape changes during Drosophila imaginal leg disc elongation: a novel morphogenetic mechanism. *Development* **111**, 23-33.

Dupont, S., Morsut, L., Aragona, M., Enzo, E., Giulitti, S., Cordenonsi, M., Zanconato, F., Le Digabel, J., Forcato, M., Bicciato, S. et al. (2011). Role of YAP/TAZ in mechanotransduction. *Nature* **474**, 179-183.

Effler, J. C., Kee, Y.-S., Berk, J. M., Tran, M. N., Iglesias, P. A. and Robinson, D. N. (2006). Mitosis-specific mechanosensing and contractile-protein redistribution control cell shape. *Curr. Biol.* **16**, 1962-1967.

Farhadifar, R., Röper, J.-C., Aigouy, B., Eaton, S. and Jülicher, F. (2007). The influence of cell mechanics, cell-cell interactions, and proliferation on epithelial packing. *Curr. Biol.* **17**, 2095-2104.

Fernández, B. G., Gaspar, P., Brás-Pereira, C., Jezowska, B., Rebelo, S. R. and Janody, F. (2011). Actin-Capping Protein and the Hippo pathway regulate F-actin and tissue growth in Drosophila. *Development* **138**, 2337-2346.

Fernandez-Gonzalez, R., Simoes, S. M., Röper, J.-C., Eaton, S. and Zallen, J. A. (2009). Myosin II dynamics are regulated by tension in intercalating cells. *Dev. Cell* **17**, 736-743.

Fink, J., Carpi, N., Betz, T., Bétard, A., Chebah, M., Azioune, A., Bornens, M., Sykes, C., Fetler, L., Cuvelier, D. et al. (2011). External forces control mitotic spindle positioning. *Nat. Cell Biol.* **13**, 771-778.

Fristrom, D. (1976). The mechanism of evagination of imaginal discs of Drosophila melanogaster. III. Evidence for cell rearrangement. *Dev. Biol.* **54**, 163-171.

Gibson, M. C., Patel, A. B., Nagpal, R. and Perrimon, N. (2006). The emergence of geometric order in proliferating metazoan epithelia. *Nature* **442**, 1038-1041.

Gibson, W. T., Veldhuis, J. H., Rubinstein, B., Cartwright, H. N., Perrimon, N., Brodland, G. W., Nagpal, R. and Gibson, M. C. (2011). Control of the mitotic cleavage plane by local epithelial topology. *Cell* **144**, 427-438.

Graner, F., Dollet, B., Raufaste, C. and Marmottant, P. (2008). Discrete rearranging disordered patterns, part I: robust statistical tools in two or three dimensions. *Eur. Phys. J. E* **25**, 349-369.

Green, A. A., Kennaway, J. R., Hanna, A. I., Bangham, J. A. and Coen, E. (2010). Genetic control of organ shape and tissue polarity. *PLoS Biol.* **8**, e1000537.

Guevorkian, K., Gonzalez-Rodriguez, D., Carlier, C., Dufour, S. and Brochard-Wyart, F. (2011). Mechanosensitive shivering of model tissues under controlled aspiration. *Proc. Natl. Acad. Sci. USA* **108**, 13387-13392.

Halder, G. and Johnson, R. L. (2011). Hippo signaling: growth control and beyond. *Development* **138**, 9-22.

Heisenberg, C. P. and Bellaïche, Y. (2013). Forces in tissue morphogenesis and patterning. *Cell* **143**, 948-962.

Huang, J., Wu, S., Barrera, J., Matthews, K. and Pan, D. (2005). The Hippo signaling pathway coordinately regulates cell proliferation and apoptosis by inactivating Yorkie, the Drosophila Homolog of YAP. *Cell* **122**, 421-434.

Klein, T. (2008). Immunolabeling of imaginal discs. *Methods Mol. Biol.* **420**, 253-263.

Kuchen, E. E., Fox, S., de Reuille, P. B., Kennaway, R., Bensmihen, S., Avondo, J., Calder, G. M., Southam, P., Robinson, S., Bangham, A. et al. (2012). Generation of leaf shape through early patterns of growth and tissue polarity. *Science* **335**, 1092-1096.

Landsberg, K. P., Farhadifar, R., Ranft, J., Umetsu, D., Widmann, T. J., Bittig, T., Said, A., Jülicher, F. and Dahmann, C. (2009). Increased cell bond tension governs cell sorting at the Drosophila anteroposterior compartment boundary. *Curr. Biol.* **19**, 1950-1955.

Lecuit, T. and Le Goff, L. (2007). Orchestrating size and shape during morphogenesis. *Nature* **450**, 189-192.

Lewis, F. T. (1926). The effect of cell division on the shape and size of hexagonal cells. *Anat. Rec.* **33**, 331-355.

Major, R. J. and Irvine, K. D. (2006). Localization and requirement for Myosin II at the dorsal-ventral compartment boundary of the Drosophila wing. *Dev. Dyn.* **235**, 3051-3058.

Mao, Y., Rauskolb, C., Cho, E., Hu, W.-L., Hayter, H., Minihan, G., Katz, F. N. and Irvine, K. D. (2006). Dachs: an unconventional myosin that functions downstream of Fat to regulate growth, affinity and gene expression in Drosophila. *Development* **133**, 2539-2551.

Mao, Y., Tournier, A. L., Bates, P. A., Gale, J. E., Tapon, N. and Thompson, B. J. (2011). Planar polarization of the atypical myosin Dachs orients cell divisions in Drosophila. *Genes Dev.* **25**, 131-136.

Marinari, E., Mehonic, A., Curran, S., Gale, J., Duke, T. and Baum, B. (2012). Live-cell delamination counterbalances epithelial growth to limit tissue overcrowding. *Nature* **484**, 542-545.

Milán, M., Campuzano, S. and García-Bellido, A. (1996). Cell cycling and patterned cell proliferation in the wing primordium of Drosophila. *Proc. Natl. Acad. Sci. USA* **93**, 640-645.

Minc, N., Burgess, D. and Chang, F. (2011). Influence of cell geometry on division-plane positioning. *Cell* **144**, 414-426.

Ni, J. Q., Markstein, M., Binari, R., Pfeiffer, B., Liu, L. P., Villalta, C., Booker, M., Perkins, L. and Perrimon, N. (2008). Vector and parameters for targeted transgenic RNA interference in Drosophila melanogaster. *Nat. Methods* **5**, 49-51.

Nishimura, T., Honda, H. and Takeichi, M. (2012). Planar cell polarity links axes of spatial dynamics in neural-tube closure. *Cell* **149**, 1084-1097.

O'Brochta, D. A. and Bryant, P. J. (1985). A zone of non-proliferating cells at a lineage restriction boundary in Drosophila. *Nature* **313**, 138-141.

Oda, H. and Tsukita, S. (2001). Real-time imaging of cell-cell adherens junctions reveals that Drosophila mesoderm invagination begins with two phases of apical constriction of cells. *J. Cell Sci.* **114**, 493-501.

Oh, H. and Irvine, K. D. (2011). Cooperative regulation of growth by Yorkie and Mad through bantam. *Dev. Cell* **20**, 109-122.

Olguín, P., Glavic, A. and Mlodzik, M. (2011). Intertissue mechanical stress affects Frizzled-mediated planar cell polarity in the Drosophila notum epidermis. *Curr. Biol.* **21**, 236-242.

Ranft, J., Basan, M., Elgeti, J., Joanny, J.-F., Prost, J. and Jülicher, F. (2010). Fluidization of tissues by cell division and apoptosis. *Proc. Natl. Acad. Sci. USA* **107**, 20863-20868.

Rauzi, M., Verant, P., Lecuit, T. and Lenne, P.-F. (2008). Nature and anisotropy of cortical forces orienting Drosophila tissue morphogenesis. *Nat. Cell Biol.* **10**, 1401-1410.

Sagner, A., Merkel, M., Aigouy, B., Gaebel, J., Brankatschk, M., Jülicher, F. and Eaton, S. (2012). Establishment of global patterns of planar polarity during growth of the Drosophila wing epithelium. *Curr. Biol.* **22**, 1296-1301.

Sansores-Garcia, L., Bossuyt, W., Wada, K.-I., Yonemura, S., Tao, C., Sasaki, H. and Halder, G. (2011). Modulating F-actin organization induces organ growth by affecting the Hippo pathway. *EMBO J.* **30**, 2325-2335.

Schwank, G., Tauriello, G., Yagi, R., Kranz, E., Koumoutsakos, P. and Basler, K. (2011). Antagonistic growth regulation by Dpp and Fat drives uniform cell proliferation. *Dev. Cell* **20**, 123-130.

Tapon, N., Harvey, K. F., Bell, D. W., Wahrer, D. C. R., Schiripo, T. A., Haber, D. A. and Hariharan, I. K. (2002). salvador Promotes both cell cycle exit and apoptosis in Drosophila and is mutated in human cancer cell lines. *Cell* **110**, 467-478.

Théry, M., Racine, V., Pépin, A., Piel, M., Chen, Y., Sibarita, J.-B. and Bornens, M. (2005). The extracellular matrix guides the orientation of the cell division axis. *Nat. Cell Biol.* **7**, 947-953.

Uyttewaal, M., Burian, A., Alim, K., Landrein, B., Borowska-Wykręt, D., Dedieu, A., Peaucelle, A., Ludynia, M., Traas, J., Boudaoud, A. et al. (2012). Mechanical stress acts via katanin to amplify differences in growth rate between adjacent cells in Arabidopsis. *Cell* **149**, 439-451.

Wartlick, O., Kicheva, A. and González-Gaitán, M. (2009). Morphogen gradient formation. *Cold Spring Harb. Perspect. Biol.* **1**, a001255.

Wartlick, O., Mumcu, P., Kicheva, A., Bittig, T., Seum, C., Jülicher, F. and González-Gaitán, M. (2011b). Dynamics of Dpp signaling and proliferation control. *Science* **331**, 1154-1159.

Yoshigi, M., Hoffman, L. M., Jensen, C. C., Yost, H. J. and Beckerle, M. C. (2005). Mechanical force mobilizes zyxin from focal adhesions to actin filaments and regulates cytoskeletal reinforcement. *J. Cell Biol.* **171**, 209-215.

Zallen, J. A. and Wieschaus, E. (2004). Patterned gene expression directs bipolar planar polarity in Drosophila. *Dev. Cell* **6**, 343-355.

Zecca, M. and Struhl, G. (2007). Recruitment of cells into the Drosophila wing primordium by a feed-forward circuit of vestigial autoregulation. *Development* **134**, 3001-3010.

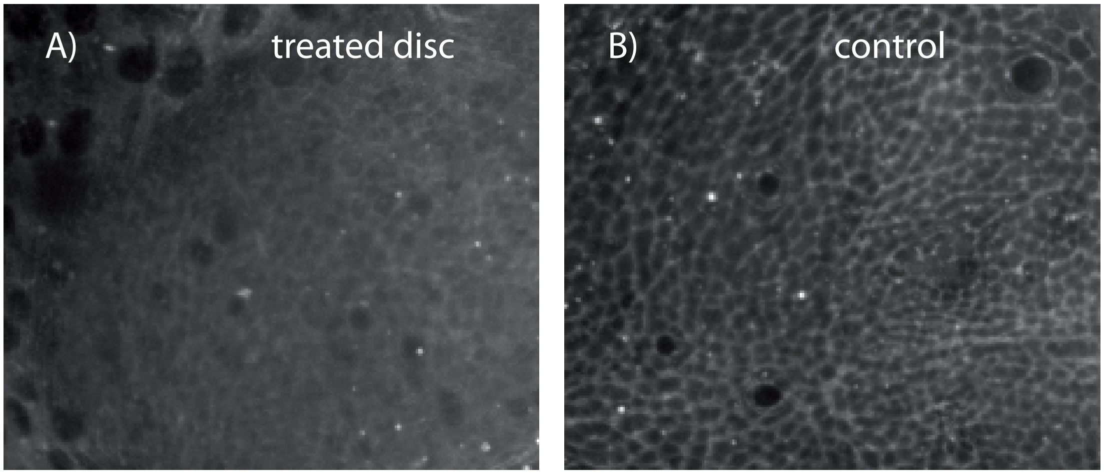
A)
treated disc
B)
control

Fig. S1. Effect of Y27632 on MyoII::GFP. (**A**) A MyoII::GFP wing disc after a 40 minutes exposure to 1 mM Y27632. (**B**) The control twin disc.

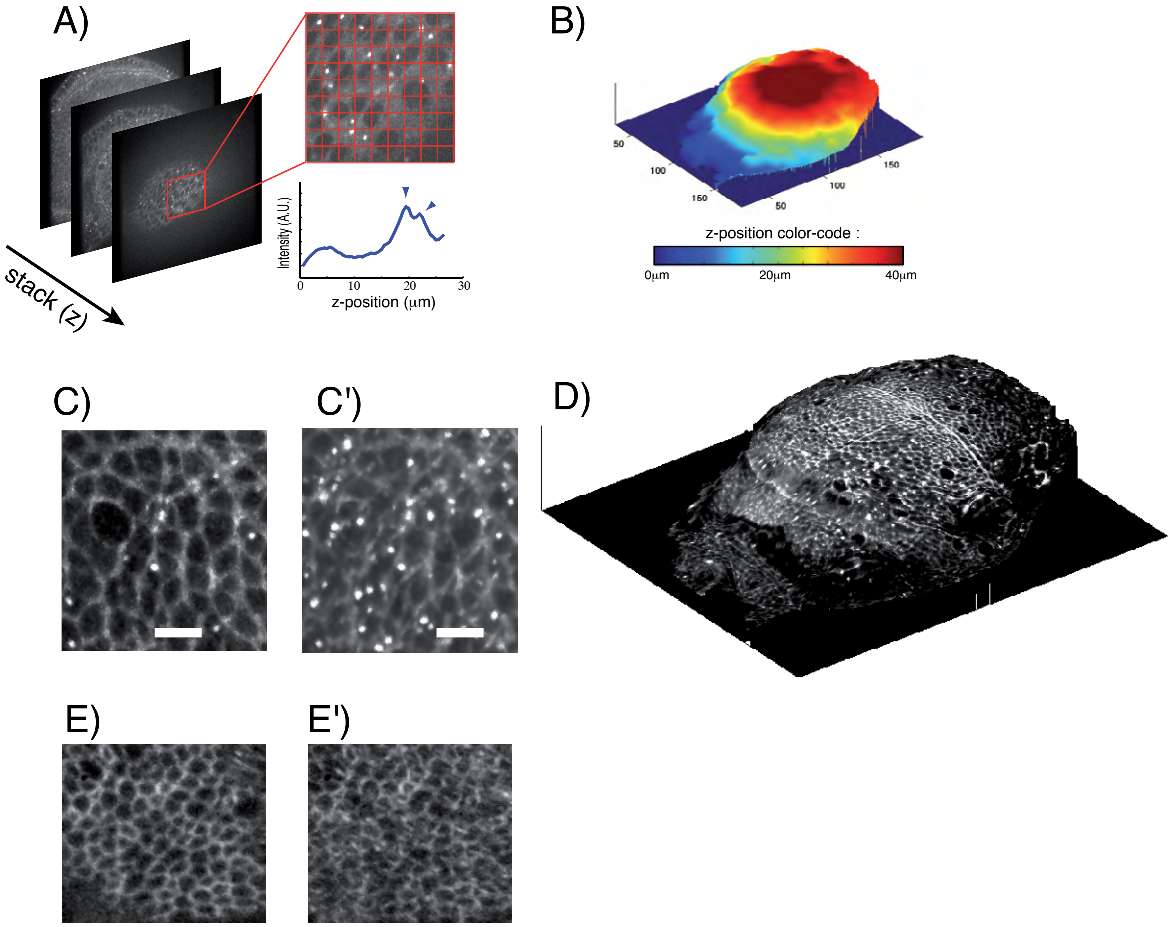
A)
stack (z)
Intensity (A.U.)
0
10
20
30
z-position (µm)
B)
50
100
150
150
100
50
z-position color-code :
0µm
20µm
40µm
C)
C')
D)
E)
E')

Fig. S2. Method for the selective plane projection. (**A**) After binning in *xy*, the intensity of a bin as a function of *z* shows two maxima corresponding to adherens junctions (AJs) of wing proper and peripodial cells. (**B**) 3D profile of wing-proper AJs. (**C**,**C′**) Selective plane projection (C) versus maximum intensity (C′) on MyoII-GFP. (**D**) 3D representation of the MyoII-GFP signal. (**E**,**E′**) Selective plane projection (E) versus maximum intensity (E′) on cad-GFP.

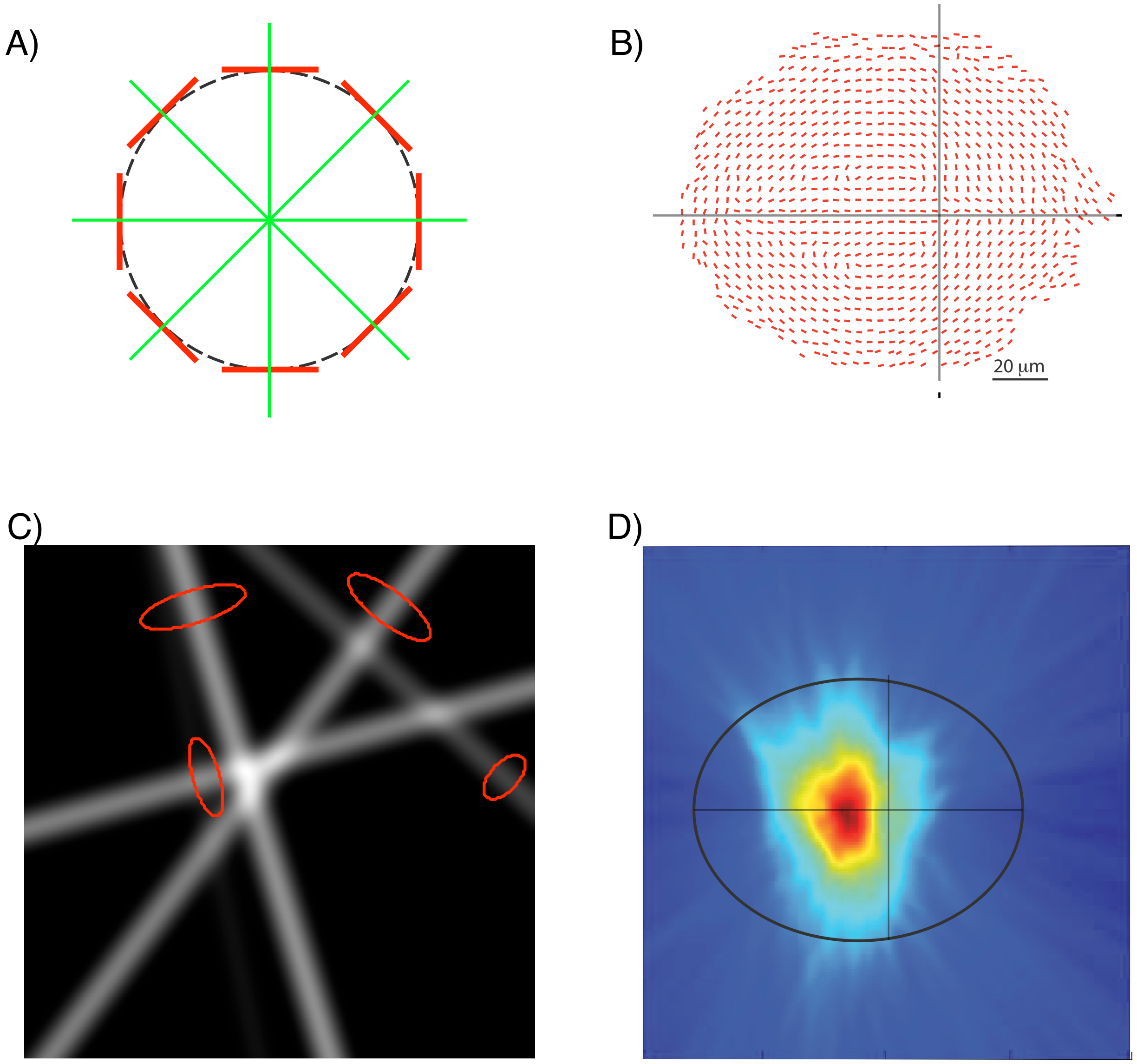

Fig. S3. Generation of the density of bisectors. (**A**) The center of a circle is found at the intersection of the bisectors (green lines) of the main axis of each cell. (**B**) The center of the pattern of orientation of the pouch can be found similarly. (**C**) The bisectors of four nearby cells. (**D**) The density of bisectors computed from the pattern of B.

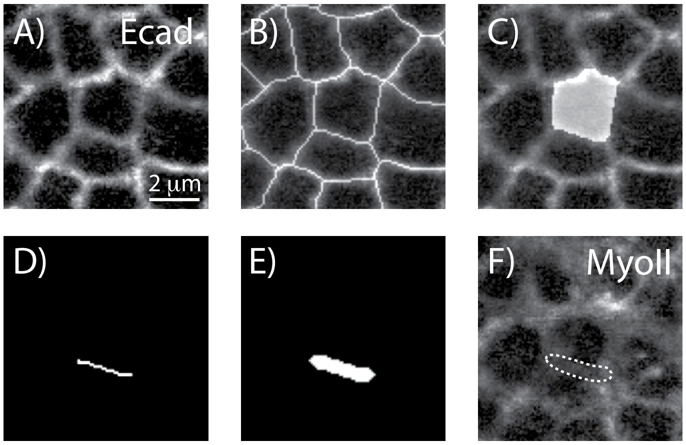

Fig. S4. Junctional enrichment analysis. (**A-C**) Ecad::GFP signal (A) overlaid with skeletonization (B) and the binary outline of one cell (C). (**D**) One cell-cell interface. (**E**) For enrichment analysis, the mask of the interface is thickened. (**F**) To measure junctional signal (here in MyoII), the average signal in the thickened junctional mask is computed.

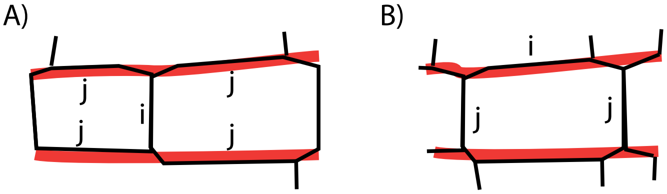

Fig. S5. Measurement of the index of polarity in MyoII cables. (**A**) Deriving the polarity index of the transverse junction i. (**B**) Deriving the polarity index of the cable junction i.

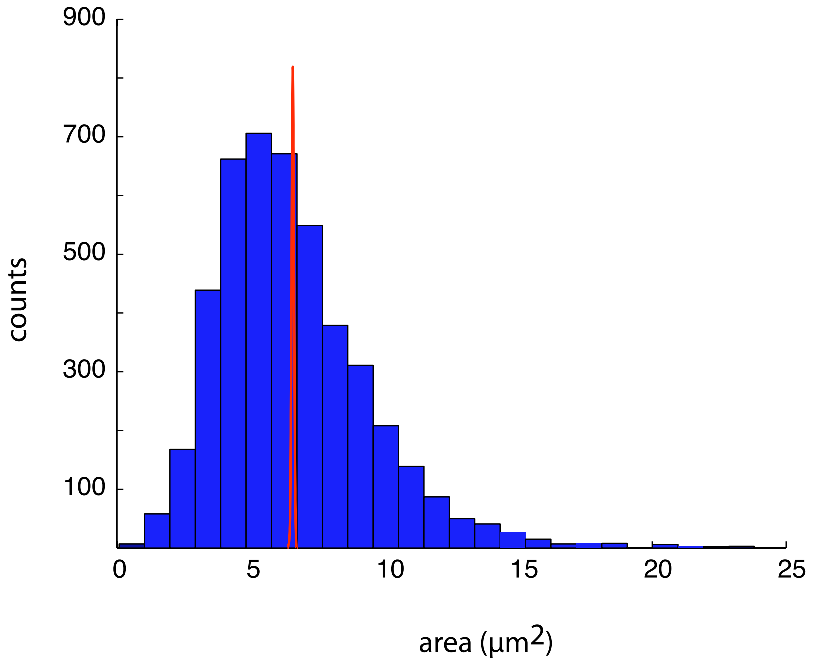

Fig. S6. Area distribution in a [34-45 μm] distance bin from the center of the pouch. The histogram shows the distribution (s.d. = 2.9 μm^2). The red curve shows the distribution of 1000 bootstrapped means (s.d. = 0.042 μm2). These data correspond to the fourth point from the left in Fig. 1B′.

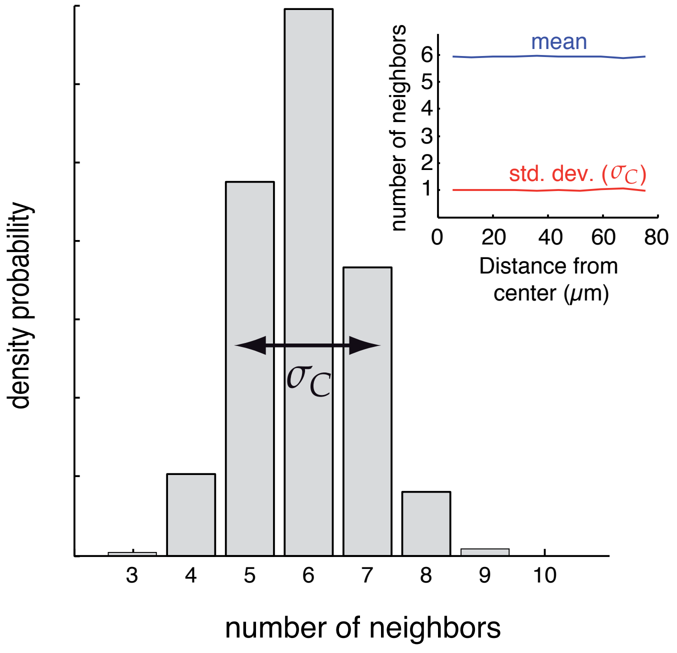

Fig. S7. Topology of cells at different locations in the tissue. The inset shows that both the mean and the width of the distribution do not significantly change as a function of the position in the tissue.

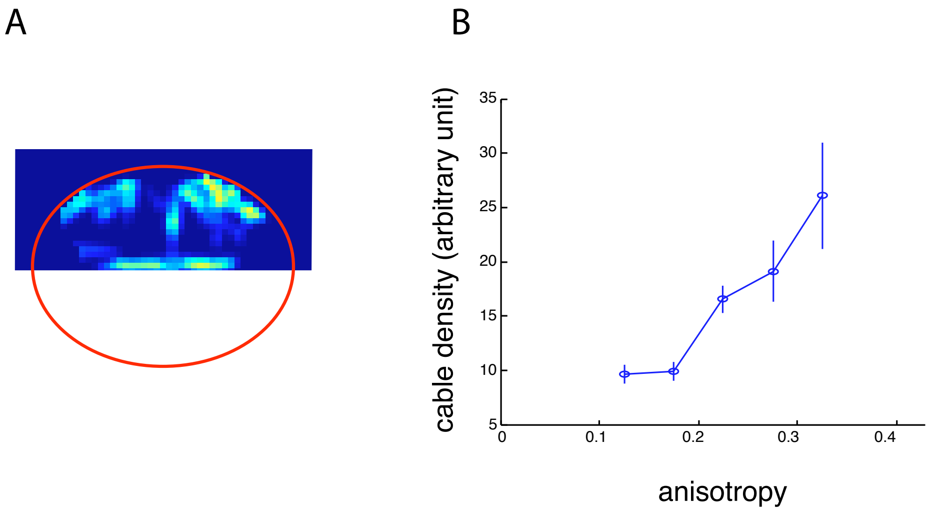

Fig. S8. MyoII cables correlate with tissue anisotropy. (**A**) The manual outline of the cables of seven pouches were register summed and low pass filtered to provide a heat map of cable density. (**B**) Anisotropy versus density of cables obtained by comparing the map of anisotropy and the map of cable density. Error bars represent s.e.m.

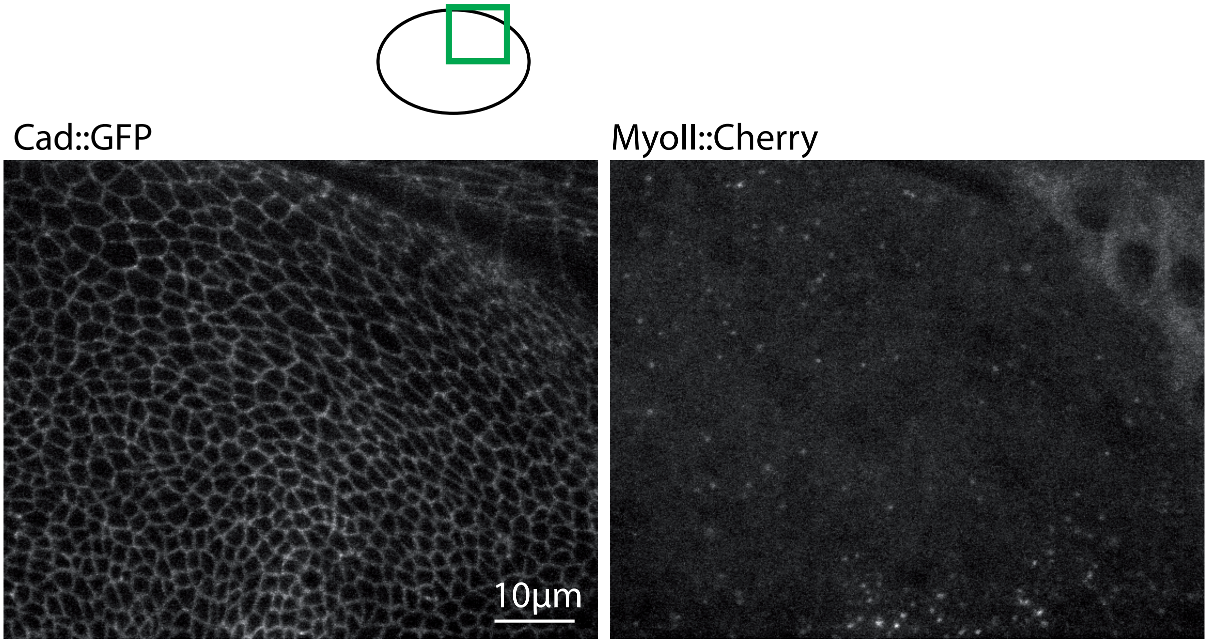

Fig. S9. Wing disc tissue after ROCK inhibitor treatment. Larger view of the disc in Fig. 5C,D, used for ablation experiments. The cartoon shows the position of the image with respect to the wing pouch. Medial cells are still smaller than peripheral ones. (**A**) Cad::GFP. (**B**) MyoII:Cherry

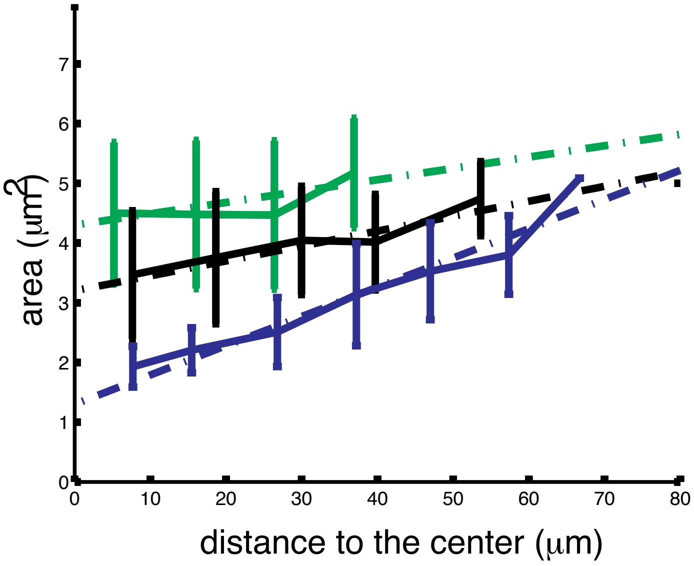

Fig. S10. Temporal evolution of the pattern of deformation. The pattern of cell area from larvae 85 hours after egg laying (AEL, green), 96 hours AEL (black), and wandering (blue) shows a gradual increase of the gradient of the cell deformation. Error bars represent s.e.m.

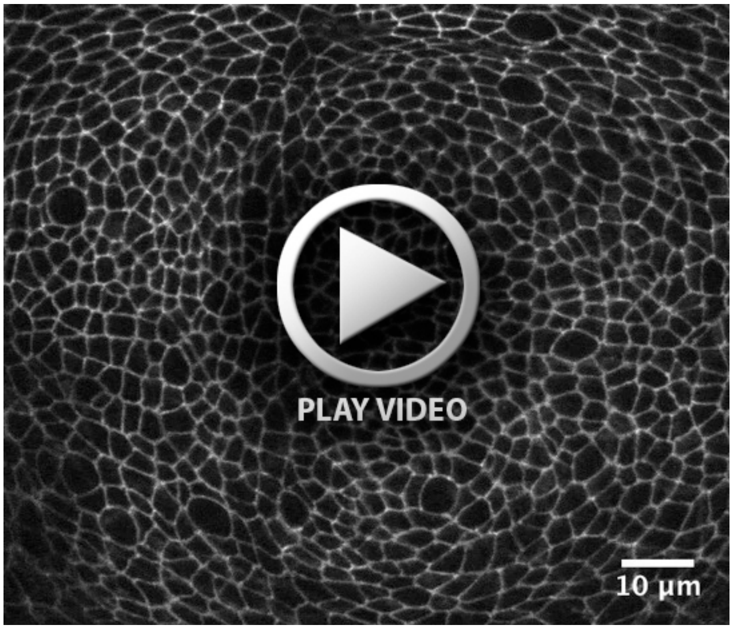

Movie 1. A time sequence of a mid-third instar wing disc imaged with a spinning disc confocal while cultured in clone 8 medium. Scale bar: 10 μm.

Movie 2 .Two examples of ablation affecting tangent junctions (red color code in Fig. 2). Scale bar: 2 µm.

Movie 3. Two examples of ablations affecting transverse junctions (blue color code in Fig. 2). Scale bar: 2 µm.

Table S1. Genotypes

	Genotype
All morphometry quantifications	*ubi-cad::GFP*
Fig. 1A	*ubi-cad::GFP*
Fig. 1C	*UAS-Gap43::Venus/+; fng-Gal4/+*
Fig. 2	*ubi-cad ::GFP*
Fig. 3B-D	*dachs-dachs::GFP*
Fig. 3E-H	*hs-flp; d*^{GC13} *FRT40A / ubi-GFP FRT40A*
Fig. 4A	*sqh*^{AX3}*; sqh-sqh::GFP; sqh-sqh::GFP*
Fig. 4B	*sqh*$^{AX3;}$*ubi-E-cad::GFP, sqh-sqh::mCherry*
Fig. 4C	*sqh*^{AX3}*; sqh-sqh::GFP ; sqh-sqh::GFP*
Fig. 4D	*dachs-dachs::GFP*
Fig. 4E	*sqh-sqh::GFP/ dachs-dachs::GFP*
Fig. 5A	*sqh*^{AX3}*; ubi-E-cad::GFP, sqh-sqh::mCherry*
Fig. 5B	*ubi-cad::GFP*
Fig. 5C	*sqh*^{AX3}*; ubi-E-cad::GFP, sqh-sqh::mCherry*
Fig. 6	*ubi-cad::GFP*
Fig. 7A-B	*hs-flp*$_{122}$*; ubi-cad::GFP /UAS-dcr2; AyGal4 UAS-RFP/UAS-expanded-dsRNA*
Fig. 7C	*hs-flp*$_{122}$*; sqh-sqh::GFP/UAS-dcr2; AyGal4 UAS-RFP /UAS-expanded-dsRNA*
Fig. 7D	*hs-flp*$_{122}$*; sqh-sqh::GFP / sqh-sqh::GFP; AyGal4 UAS-RFP/UAS-Yki*
Fig. 7E	*hs-flp; AyGal4 UAS-GFP/+; AyLexA LexAop-mCD8::GFP/UAS-Yki*
Fig. S1	*sqh*^{AX3}*; sqh-sqh::GFP; sqh-sqh::GFP*
Fig. S2A-D	*sqh*^{AX3}*; sqh-sqh::GFP; sqh-sqh::GFP*
Fig. S2E	*ubi-cad::GFP*
Fig. S8	*sqh*^{AX3}*; sqh-sqh::GFP; sqh-sqh::GFP*

Appendix S1. Image analysis

Selective plane projection

The forces that drive epithelial morphogenesis originate mainly at the level of apical junctions (AJs), which are enriched in adhesive proteins and acto-myosin cortex. We thus focus our attention on the uppermost part of epithelia, at or near AJs. The traditional approach, which consists in taking the maximum intensity projection of the stack is not optimal because it reveals bright structures that lie outside of apical junctions (such as MyoII clusters that are especially frequent in proliferating tissue due to mitotic scars), and discard dim structure of the adherens junction. This consequently reduces signal to noise ratio of the 2D projection. Furthermore, this approach ignores the 3D disposition of the 2D epithelium that might be important (*ie* curvature). We perform a selective plane projection that alleviate these issues by extracting the relevant signal exclusively from the adherens junctions, yielding a much higher signal to noise ratio. This selective plane projection (SPP) takes into account the 3D structure of the tissue.

We start from a 3D image of a wing disc. Each xy plane is then coarse grained in larger bins:

$$I_b(i,j,z) = \sum_{x=Bi}^{B(i+1)-1} \sum_{y=Bj}^{B(j+1)-1} I\,(x,y,z) \tag{1}$$

where I_b and I are the binned and unbinned image respectively, B is the bin size (equal to 20 unless otherwise specified), (i,j) and (x,y) are the positions in the binned and unbinned images respectively and z the position of the plane in the 3D stack. The inset in Fig. S2A in supplementary material shows how $I_b\ (i,j,z)$ varies with z. We distinguish two local maxima (arrowheads), which correspond to the apical junctions (which are enriched in MyoII) of the closely apposed wing disc proper and peripodial epithelium. We are interested in the former, the profile of which, $Z_{adh}(i,j)$, is then computed by local maximum finding. The coarse grained profile $Z_{adh}(i,j)$ is then refined by linear interpolation up to the original resolution of $I(x,y,z)$ (see Fig. S2B for a 3D rendering of the profile). The selective plane projection (SPP) then consists in taking the fluorescent intensity along the apical junction profile $I_{spp}(x,y) = I(x,y,Z_{adh}(i,j))$. Fig. S2C compares the same stack projected with SPP and maximum intensity. Warping $I_{spp}(x,y)$ onto the $3D$ profile of the tissue $Z_{adh}(i,j)$ generates a 3D visualization (Fig. S2D). Fine details of the tissue, such as dividing cells or actomyosin cables that span compartment boundaries, can now be apprehended in a 3D context. SPP allows the observation of cad::GFP signal in the periphery of the wing disc with much better clarity than a maximum intensity projection (Fig. S2E $vs.$ Fig. S2E')

Skeletonization of tissues

Noise was removed from the images using a median filter. Images were then skeletonized using a crest finding algorithm (Steger, 1998). The subsequent skeleton comprised many small defects consisting of either small holes in a junction or extra segment with loose ends. The former were first corrected by applying closing morphological transformation, the latter were then corrected by applying to the binary skeleton a convolution filter of kernel $\begin{pmatrix} 1 & 1 & 1 \\ 1 & 0 & 1 \\ 1 & 1 & 1 \end{pmatrix}$, which attributes the value 1 to the ends of segment. Applying a threshold > 1 and reiterating the procedure shortens loose ends. The skeletons were eventually visually compared to the raw cad::GFP projections and manually corrected.

Texture analysis

Average orientation and anisotropy of tissue was quantified using the texture tensor introduced in (Graner et al., 2008), and defined locally for cell i by the matrix :

$$M_i = \frac{1}{N_i} \sum_{j=1}^{N_i} \begin{pmatrix} \Delta x_{ij}{}^2 & \Delta x_{ij} \Delta y_{ij} \\ \Delta x_{ij} \Delta y_{ij} & \Delta y_{ij}{}^2 \end{pmatrix} \qquad (2)$$

where j stands for the successive neighbors of cell i, N_i its total number of neighbors, Δx_{ij} (resp. Δy_{ij}) is the x-coordinate (resp. y-coordinate) of the link joining the centers of mass of cell i and cell j. We performed a first order correction for the effect of tissue curvature and non flatness on texture by realizing that curvature occurs on a spatial scale much larger than the size of a cell. Thus the tissue can be considered as locally flat. A 2D texture matrix around each cell, was thus computed using the local best planar approximation. 3D positions of the center of mass of cells, a pre-requisite of the local correction, was obtained by a combination of the 2D skeleton of cells in the tissue and the 3D profile of the tissue $Z_{adh}(x, y)$, output from the selective plane projection we developed. The eigenvectors of tensor (2), $\overrightarrow{u_{max}^i}$ and $\overrightarrow{u_{min}^i}$, give the orientations of the major and minor axis of the tissue around cell i. The square root of the eigenvalues of tensor (2) give the corresponding length scale λ_{max}^i and λ_{min}^i. The local anisotropy around cell i, a_i, is then defined by :

$$a_i = \left(\frac{\lambda_{max}^i - \lambda_{min}^i}{\lambda_{max}^i + \lambda_{min}^i} \right) \qquad (3)$$

Statistical morphometry

In order to remove intrinsic noise of the cellular lattice, morphometric measurements were averaged in bins of size=5-15μm within one disc, as well as averaged over 15 discs. The contour of the pouch is simply delineated by the existence of the deep folds around it, at stages posterior to 85h after egg laying. Before the presence of the folds (green in Fig.S8) the pouch can be delineated by the expression of a vestigial Qadrant enhancer reporter (Zecca & Struhl, 2007). Successive discs were registered spatially by using the antero-posterior and dorso-ventral compartment boundaries as landmarks to rotate and translate wing discs so as to superimpose them. Both compartment boundaries are clearly visible when imaging cad::GFP on living wing discs, because cell reproducibly align along these straight boundaries by a mechanism that is associated to a recruitment in MyoII (Landsberg et al., 2009; Major & Irvine, 2006). Averaging of the morphometry is simply done by computing an averaged texture tensor (2) and computing its eigenvectors and eigenvalues. The output of this statistical morphometry is a collection of maps of averaged morphometry (apical area, orientation, anisotropy). For an easier comparison with modeling, and because we find a polar symmetry in our maps (see main body of the text), these 2D maps were reduced to 1D curves by binning pixels as a function of their distance to the geometric center of the tissue (as measured from the maximum of the density of bisectors, see below) and averaging their value within each distance-bin.

Density of bisectors

In order to estimate the overlap of the pattern of local orientation (Fig. 1E) and the pattern of apical area (Fig. 1B), we transform the collection of vectors given by the map of orientation analysis into an image that encodes the probability for a pixel to be at the center of the orientation pattern of these vectors. The transformation is done by simply drawing the bisectors of all the vectors. This approach can be illustrated by considering a set of vectors that are aligned along a perfect circle (Fig. S3A in supplementary material). The center of the pattern is the center of the circle, and can be found at the intersection of the bisectors of the vectors (green line on Fig. S3A). In the more disordered case of the wing disc (Fig. S3B), bisectors do not meet at a unique point, nonetheless the zone of maximum intensity of the density of bisectors can be considered as the center of the pattern. The transformation to go from a collection of vectors to the density of bisectors is done as follows: The image of the density of bisector is the sum of all the bisectors of the main axis of cells (as defined by the local texture) weighted by their anisotropy, and convolved with a gaussian blur to provide some spatial averaging. The intensity of this density of bisector on any point M is thus given by the formula:

$$I(M) = \sum_{k=1}^{N_{total}} \left(\frac{\lambda_{max}^k - \lambda_{min}^k}{\lambda_{max}^k + \lambda_{min}^k}\right) exp\left(-\frac{\|\overrightarrow{OM}\cdot\overrightarrow{u_{max}^k}\|^2}{\sigma^2}\right) \quad (4)$$

where N_{total} is the total number of cells analyzed, λ_{max}^k and λ_{min}^k are the characteristic distances along the major and minor axis of the kth cell. O_k is the position of the kth cell, and $\overrightarrow{u_{max}^k}$ is the unit vector giving the local orientation around the kth cell (technically, the normalized eigen vector of the largest eigen value of the texture tensor). σ is the characteristic distance of the gaussian blur (σ=4μm). Fig. S3C shows the bisector of 4 cells, Fig. S3D show the result for all cells analyzed.

Analysis of junctional enrichment of MyoII and E-cad

The output of the skeletonization procedure is an ensemble of surfaces corresponding to the cells separated by a one pixel thick contour (Fig. S4A-C in supplementary material). Each cell is labeled, and the list of its neighbor is determined by finding those cells that overlap with it when all cells are dilated by convolution of their binary mask with the following kernel, which broadens cells by 2 pixels:

$$\begin{pmatrix} 0 & 0 & 1 & 0 & 0 \\ 0 & 1 & 1 & 1 & 0 \\ 1 & 1 & 1 & 1 & 1 \\ 0 & 1 & 1 & 1 & 0 \\ 0 & 0 & 1 & 0 & 0 \end{pmatrix} \quad (5)$$

A junction is then simply defined as the intersection of two neighbor-cells that have been dilated with the kernel 5 (Fig. S4D). The cortical enrichment of a junction (MyoII or E-Cad labeling) is subsequently measured by taking the average signal in a surface corresponding to the junction dilated with the kernel 5 (Fig. S4E-F), and subtracting the background value at the center of the cell. When required, the angle of a junction is obtained from the axis of least second moment. To assess the angular distribution of junctional enrichment, we computed the relative intensity of junctions, normalized by the mean :

$$I_i^r = \frac{I_i - \langle I \rangle}{\langle I \rangle} \quad (6)$$

where I_i^r is the relative intensity in angular bin i, I_i is the averaged intensity of junctions in angular bin i, $\langle I \rangle$ is the intensity averaged over all angular bins. To assess the angular distribution of junctional length, we computed the relative length of junctions, normalized by the mean :

$$L_i^r = \frac{L_i - \langle L \rangle}{\langle L \rangle} \quad (7)$$

where L_i^r is the relative summed length in angular bin i, L_i is the sum of the length of all junctions in the angular bin i, $\langle L \rangle$ is the summed length averaged over the angular bins.

The index of polarity used to analyze ablation experiments in MyoII cables and their transverse dim counterparts was computed with

$$P^i = \frac{I_{junct}^i - < I_{junct}^j >_j}{< I_{junct}^j >_j} \quad (8)$$

where $<>_j$ denotes the average over j, the neighboring junctions of the junction i analyzed as depicted on Fig. S5A-B